Residual Strain and Fracture Response of Al$_2$O$_3$ Coatings Deposited via APS and HVOF Techniques

R. Ahmed, N.H. Faisal, A.M. Paradowska, and M.E. Fitzpatrick

The aim of this investigation was to nondestructively evaluate the residual stress profile in two commercially available alumina/substrate coating systems and relate residual stress changes with the fracture response. Neutron diffraction, due to its high penetration depth, was used to measure residual strain in conventional air plasma-sprayed (APS) and finer powder high velocity oxy-fuel (HVOF (θ-gun))-sprayed Al$_2$O$_3$ coating/substrate systems. The purpose of this comparison was to ascertain if finer powder Al$_2$O$_3$ coatings deposited via θ-gun can provide improved residual stress and fracture response in comparison to conventional APS coatings. To obtain a through thickness residual strain profile with high resolution, a partially submerged beam was used for measurements near the coating surface, and a beam submerged in the coating and substrate materials near the coating-substrate interface. By using the fast vertical scanning method, with careful leveling of the specimen using theodolites, the coating surface and the coating/substrate interface were located with an accuracy of about 50 μm. The results show that the through thickness residual strain in the APS coating was mainly tensile, whereas the HVOF coating had both compressive and tensile residual strains. Further analysis interlinking Vickers indentation fracture behavior using acoustic emission (AE) was conducted. The microstructural differences along with the nature and magnitude of the residual strain fields had a direct effect on the fracture response of the two coatings during the indentation process.

Keywords	acoustic emission, alumina, fracture toughness, indentation, neutron diffraction, residual stress, thermal spray coating

1. Introduction

Thermal spraying of alumina (Al$_2$O$_3$) powders is widely used in surface modification technology to improve the performance and quality of engineering components in harsh environments requiring thermal, electrical, and wear resistance. A major factor dictating the performance (notably cohesive and adhesive strengths) of thermal spray coatings is residual stress, generated during coating deposition due to the fast quenching of coating powder particles and differences in the coefficient of thermal expansion (CTE) of the coating/substrate system (Ref 1-3). Phase transformations during coating deposition further influence this stress field (Ref 4, 5).

R. Ahmed and **N.H. Faisal**, School of EPS, Heriot-Watt University, Edinburgh EH14 4AS, UK; and College of Engineering, Alfaisal University, Riyadh 11533, Kingdom of Saudi Arabia; **A.M. Paradowska**, Rutherford Appleton Laboratory, ISIS, Didcot OX11 0QX, UK; **M.E. Fitzpatrick**, Materials Engineering, The Open University, Milton Keynes MK7 6AA, UK. Contact e-mail: R.Ahmed@hw.ac.uk.

Recent advancements in the high velocity oxy-fuel (HVOF) technique have made it possible to deposit much finer Al$_2$O$_3$ powders (θ-gun) at much lower temperatures than those achieved by plasma spraying processes (Ref 6, 7). This has the effect of limiting phase transformations during coating deposition, which along with the higher velocity and lower temperature of HVOF can influence residual stress. Investigations relating to the influence of powder particle size on the residual stress of thermal spray coatings have indicated that the decrease in powder particle size increases the residual stress in thermal spray deposits (Ref 8, 9). Measurement of residual strains in these thermal spray coatings is critical for modeling and designing improved components. The influence of coating powder characteristics, spraying process, and spraying process parameters on the residual stress field of Al$_2$O$_3$ coatings has also been the topic of recent investigations (Ref 10-18).

Nondestructive through thickness residual strain measurements in thermal spray coatings is possible via the high penetration depth achieved by the neutron diffraction technique (Ref 2-4). In addition to neutron-based strain measurements, there have been some other limited studies on the use of nondestructive techniques to study the structure-property relationships, e.g., using acoustic emission (AE) to investigate the fracture response during indentation of plasma-sprayed Al$_2$O$_3$ coatings; where pore coalescence, fracture, deformation, debonding, and densification in coatings have been investigated (Ref 19, 20). The influence of thermally sprayed cermet and ceramic

Nomenclatures

a	Average Vickers indentation half-diagonal size
A_{sg}	Ratio of signal gain
c	Average radial crack length $c = l_a + a$
d_{hkl}	Lattice interplanar spacing
d_{hkl}^0	Strain-free lattice interplanar spacing
E	Acoustic emission energy
E_s	Elastic modulus of specimen
$E_{c,s}$	Elastic modulus of coating and substrate
E_r	Reduced elastic modulus
K_{1c}	Fracture toughness
k_{AE}	AE-based empirical constant
L	Total surface crack length
l_a	Average surface-radial crack length
P	Indentation load
p_1	Center of specimen
p_2	Distance from center of specimen
R	Ring-down count
R_a	Surface roughness
h_f	Final penetration depth
h_{max}	Maximum penetration depth
l	Original length
T	Event duration
ΔT	Temperature change
t	Time
U_{op}	Output signal amplitude
U_{ip}	Input signal amplitude
V_{abs}	Absolute voltage
V_t	Threshold voltage
x	Change in length

Greek Symbols

α	Phase of material composition
α_{CTE}	Coefficient of thermal expansion
γ	Phase of material composition
ε	Elastic strain
σ	Stress
ν	Poisson's ratio

Subscripts

abs	Absolute
c	Coating
f	Final
hkl	Lattice planes
I	Indentation
ip	Input
max	Maximum
op	Output
R	Residual
s	Specimen or surface

Abbreviations

AE	Acoustic emission
APS	Air plasma spray
C	Through thickness coating section
CS	Coating surface
CTE	Coefficient of thermal expansion
dB	Decibel
HVOF	High-velocity oxygen fuel
S	Substrate section near surface
ESEM	Environmental scanning electron microscopy
XRD	X-ray diffraction

coating materials on the indentation behavior has also been a topic of research in recent investigations (Ref 21-24).

The aim of this study was to ascertain the relative changes in the residual stress profile and fracture response in two commercially available thermally sprayed Al_2O_3 coatings. This comparison was based on conventional APS and finer powder HVOF (θ-gun) coatings to ascertain if finer powder coatings can provide improved residual stress and fracture response. Residual stress results are related to AE-monitored Vickers indentation fracture behavior with a view to providing an indirect measure of the coating's quality.

2. Materials and Methods

2.1 Coated Test Specimens

The properties of the processed Al_2O_3 powders used and coating deposition conditions are listed in Table 1. The processed powder used sizes which ranged between 10 and 45 μm for the APS Al_2O_3 (conventional powder) coatings and 1-5 μm for the HVOF Al_2O_3 (fine powder) coatings, both of which had angular and irregular morphology (Fig. 1). Thermal spraying was done using 9 MB for APS and θ-gun for HVOF coating using industrially optimized process parameters (Ref 7) to produce an average coating thickness of 250 μm, deposited on one side of AISI 440C martensitic stainless steel (C: 0.86-1.20; Mn: 1.0 max.; Si: 1.0 max.; P: 0.04 max.; S: 0.03 max.; Mo: 0.75 max.; Cr: 16.0-18.0; Fe: balance) discs of diameter 31 mm and thickness 8 mm. Prior to spraying, the substrate was grit-blasted and cleaned to improve coating adhesion.

For the nanoindentation testing, the coated specimens surface and cross section surface were ground and polished using SiC paper and diamond paste to an average surface roughness (R_a) of 0.27 ± 0.02 for APS and 0.096 ± 0.02 for HVOF coatings. For the Vickers indentation test (Ref 25), the coated specimen surfaces were ground and polished to an average coating thickness of 220 μm.

Table 1 Thermal spray process parameters

Thermal spray gun	Spray conditions and powders	
9-MB Metco (APS)	Spray material	Conventional alumina ($Al_2O_3 > 98.0\%$)
	Powder size	10-45 μm
	Arc current	500 A
	Arc voltage	70 V
	Primary gas	37.6 L/min (Ar)
	Secondary gas	7.1 L/min (H_2)
	Spray distance	80 mm
	Coating thickness	250 μm
θ-Gun (HVOF)	Spray material	Fine powder alumina ($Al_2O_3 > 98.0\%$)
	Powder size	1-5 μm
	Oxygen flow rate	893 L/min
	Kerosene flow rate	0.32 L/min
	Acetylene flow rate	43 L/min
	Spray distance	150 mm
	Coating thickness	250 μm
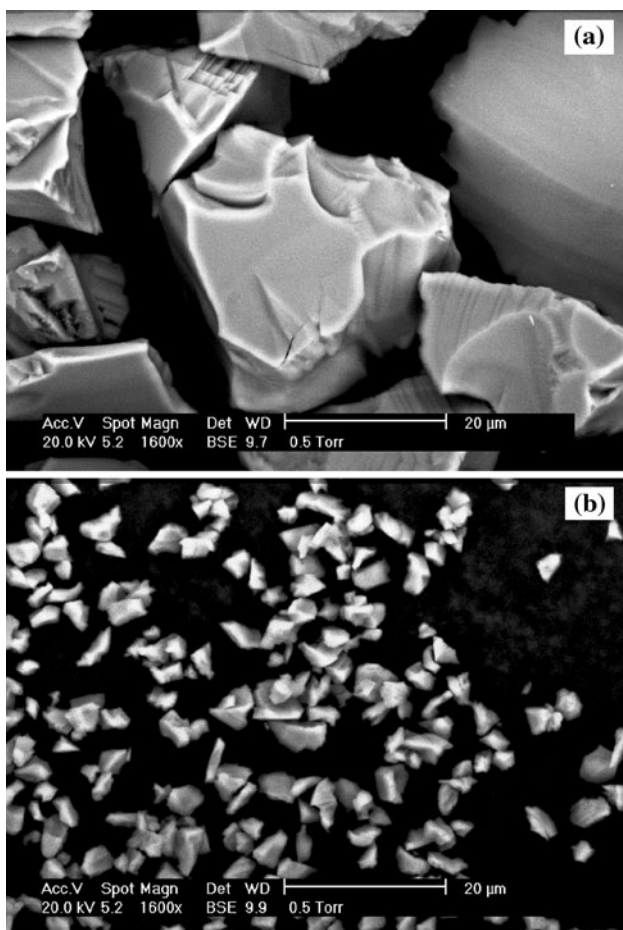
Fig. 1 Powders: (a) 10-45 μm for APS Al_2O_3 (conventional powder) coatings for APS and (b) 1-5 μm for HVOF Al_2O_3 (fine powder) coatings

2.2 Microstructural Characterization

Coating microstructure was investigated via cryogenic fracture in liquid nitrogen to reveal coating porosity and splat morphology. Coating flakes were removed from substrates which were refrigerated in liquid nitrogen and broken by bending in a direction perpendicular to the coating surface. The microstructure of the coatings was examined by environmental scanning electron microscopy (ESEM). Coating porosity on polished cross sections was measured using image analysis software (Buehler OmniMet®).

2.3 Nanoindentation Measurements

Nanoindentation experiments at 100 mN load were carried out to obtain the elastic modulus and hardness using a calibrated TriboIndenter® (Hysitron Inc., MN) equipped with a Berkovich indenter. Experiments were conducted using a force-displacement sequence. For each loading-unloading cycle, loading and unloading lasted 15 s, respectively, and a dwell time of 5 s at each peak load was used. Ten measurements were performed on each coating surface and 40 on each cross section, which were distributed in four lines of 10 measurement points each, at 50, 100, 150, and 200 μm, respectively, from the coating's surface. Similarly, 20 measurements were performed on each substrate cross section near the interface, which were distributed in two lines of 10 measurement points each, at 50 and 100 μm, respectively, from the interface. Indentations were spaced >2.5 times the diagonal apart (Ref 25), to avoid any interaction between the sinking-in, piling-up, surface and subsurface lateral cracks of neighboring indentations (Ref 22). The raw data were then used to construct the load-displacement plot and evaluated based on the Oliver and Pharr method (Ref 26).

2.4 X-ray Diffraction and Measurement of Neutron Diffraction Residual Strain and Stress

X-ray diffraction (XRD) analysis was used to reveal the crystalline phase composition of the coatings. A Bruker AXS, Model D8 ADVANCE X-Ray diffractometer was used operating at 40 kV and 40 mA. Cu K_α radiation was used (wavelength, $\lambda = 0.1542$ nm) and the goniometer was run from 5.0° to 84.9° with a step size of 0.009° (2θ) at 15.4 s per step.

Neutron diffraction strain measurements were performed at the UK ISIS Facility, using the ENGIN-X strain measurement diffractometer (Ref 2-4). This is a pulsed neutron diffractometer equipped with slits and collimators to achieve small gage volumes (Ref 27). The experiments were conducted in vertical scan mode (Fig. 2) to measure through thickness residual strain profile of the coating-substrate system and the gage volume height of the order of 300-400 μm was used (Ref 28). The details of the vertical scan method are described elsewhere (Ref 2). Strain measurements were performed at the center of the specimen (at p_1) and also at a radial distance, $r = 5$ mm (at p_2) from the center, as shown schematically in Fig. 2. Although the measurement locations in the specimen were changed, the distance to the detectors (Bank 1 and Bank 2) was always the same. To achieve a through thickness residual strain profile with high resolution, a partially submerged beam was used for measurements
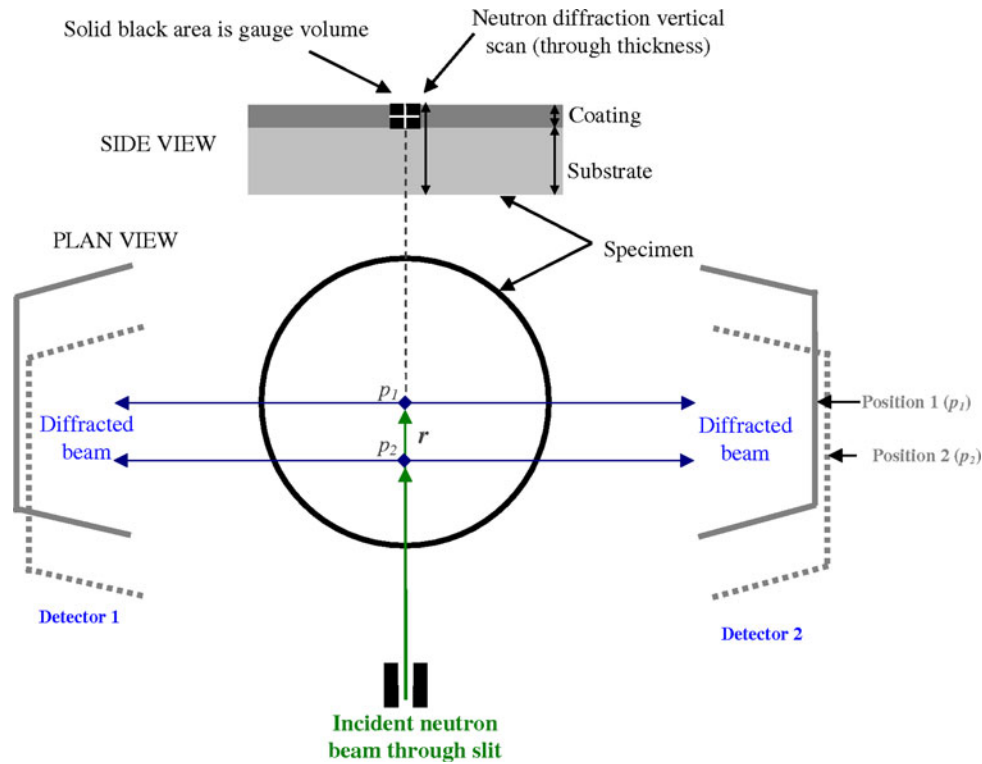
Fig. 2 Schematic of measuring residual strain using neutron diffraction

near the coating surface, and a beam submerged in the coating and substrate materials near the coating-substrate interface. Further details of the partially submerged beam technique to measure strain at a volume resolution finer than the height of the gage volume can be appreciated from Edwards (Ref 28). By using the fast vertical scan and careful leveling of the specimen using theodolites, the coating surface and the coating-substrate interface was located with a resolution of about 50 μm.

The residual strain was obtained from the shift in individual Al_2O_3 (α, γ) and Fe (α) peaks for the coating and substrate materials, respectively, using a single peak fitting routine (Ref 29). The peaks chosen for the strain analysis within each coating material were such that the peaks had none or minimum overlap with other peaks. The strain-free lattice parameter (d_{hkl}^0) for the coating material was obtained by carefully removing the coating from the substrate and crushing the deposit to form a powder. This powder was then put in a vanadium tube and its lattice parameter measured. The strain-free lattice parameter for the steel substrate was measured at the uncoated surface of the substrate disc. The direct elastic strain in the material at the measured direction was calculated from Eq 1:

$$\varepsilon_{hkl} = \frac{d_{hkl} - d_{hkl}^0}{d_{hkl}^0}, \tag{Eq 1}$$

where d_{hkl} is the measured interplanar lattice spacing and d_{hkl}^0 is the stress-free interplanar spacing for the material.

The elastic stress was calculated from these strain values using the through thickness elastic modulus value.

2.5 Vickers Indentation Fracture and AE Measurements

This set of experiments consisted of producing indentations using a conventional Vickers hardness testing machine at nine different loads between 98 and 490 N with a single AE sensor mounted on the coated surface. Five indentations were produced at each load and the total surface crack pattern was subsequently measured for all indentations. Further details of this measurement technique can be found elsewhere (Ref 21-23).

For the purposes of making an assessment of the correlation between AE and cracking, one can suppose that the energy associated with the AE is approximately proportional to the area of new crack surface formed. Continuous background noise was present throughout the study, so an automatic analysis threshold level of 15% above the continuous background noise level was chosen to define significant AE activity. This threshold level was based on the signal-to-noise ratio of AE data recorded during various experiments conducted in this study. The AE energy (E) was calculated as the area under the absolute of the signal above threshold (Fig. 3) using Eq 2 (Ref 21):

$$E = \int_{t=0}^{t} (V_{abs} - V_t)dt \quad \text{if } (V_{abs} - V_t) > 0, \tag{Eq 2}$$
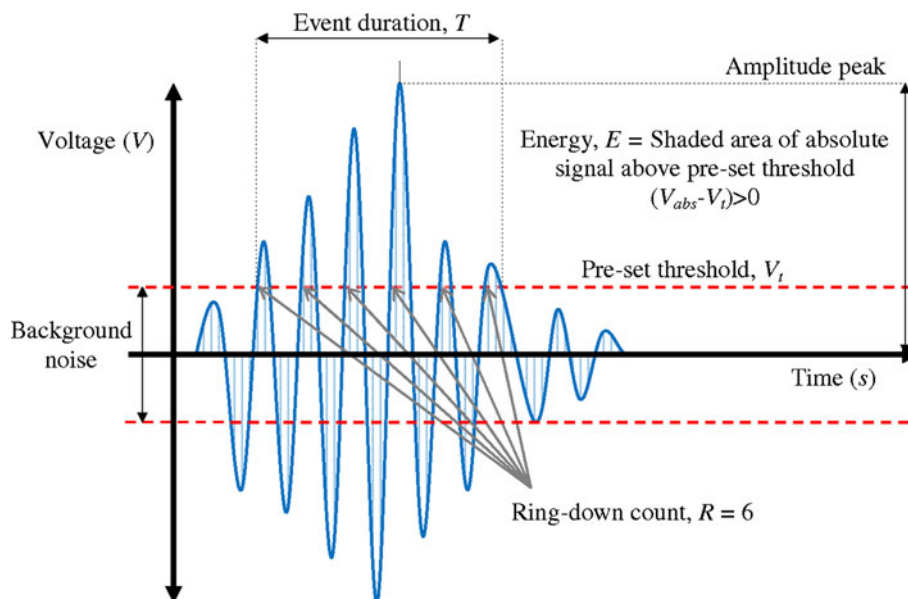
Fig. 3 Schematic diagram of a single event AE waveform showing calculation of the AE features: ring-down count R, energy E, and event duration T

where V_{abs} is the absolute voltage, V_t is threshold voltage, and t is the time (above threshold) from the beginning of the event. The event duration (T) is the total time that the signal spends above threshold, and ring-down count (R) is the number of times the signal exceeds a counter threshold. In such analysis, overlapping events are not distinguished from each other, although this will only have an effect on ring-down count and event duration, and not on energy. Prior to any signal processing all data was corrected for gain in the data acquisition system using Eq 3 (Ref 30).

$$A_{sg} = 20 \log \left(\frac{U_{op}}{U_{ip}} \right), \qquad \text{(Eq 3)}$$

where A_{sg} is signal gain expressed in dB and U_{op}/U_{ip} is the ratio of output to input signal amplitudes.

According to the various published analyses of the indentation of brittle materials, the main types of cracking observed are either surface-radial cracks (Palmqvist cracks), or radial-median cracks (Half-penny cracks). Nihara et al. (Ref 31) have distinguished between the two in terms of the classical dimensions a, l_a, and c: Palmqvist cracks, $l_a/a \leq 2.5$ or $c/a \leq 3.5$ and half-penny cracks, $c/a \geq 2.5$ (Ref 32). In this study, the average value of l_a/a and c/a were well within the Palmqvist régime. Shetty et al. (Ref 33) have devised an empirical model for Palmqvist cracks, which allows the fracture toughness (in units MPa m$^{1/2}$) of the coating to be determined from the load and crack dimensions (Eq 4):

$$K_{1c} = 0.0319 \left[\frac{P}{a\sqrt{l_a}} \right], \qquad \text{(Eq 4)}$$

where P is the indentation load (in N), a is the average indent half-diagonal size, and l_a is the average of the radial corner crack lengths, both in meters. The above formula for the determination of fracture toughness assumes that the surface is initially stress free.

3. Results

3.1 Coating Microstructure

Scanning electron microscopic images of the APS and HVOF Al$_2$O$_3$ coatings are presented in Fig. 4. The sprayed surfaces (Fig. 4a and 4b) show that the molten Al$_2$O$_3$ droplets have spread significantly and it is not possible to distinguish any nonmelted or semimolten particles. Polished coating cross sections (Fig. 4c and 4d) show a qualitatively higher porosity for the APS Al$_2$O$_3$ (conventional) than HVOF Al$_2$O$_3$ (fine powder). Coating porosity was measured as 2.8% $\pm$ 0.64 and 8.8% $\pm$ 2.0 for the HVOF and APS coatings, respectively. The thickness of individual splats corresponding to a lamella was typically between 1 and 2 μm. A columnar grain structure was observed in individual lamellae.

3.2 Nanoindentation Testing

The results obtained from the Oliver and Pharr method (Ref 26) will be invalid if the area function used to calculate the contact area between the indenter and the material in this model is incorrect (Ref 34). To verify the applicability of the Oliver and Pharr method (Ref 26), it is necessary to calculate the (h_f/h_{max}) ratio from the load-displacement (P-h) curve, where h_f is final penetration depth (residual) and h_{max} is maximum penetration depth. The value of this ratio should lie below 0.7 to obtain reliable results from the Oliver and Pharr method (Ref 26). The average values of (h_f/h_{max}) ratio for the
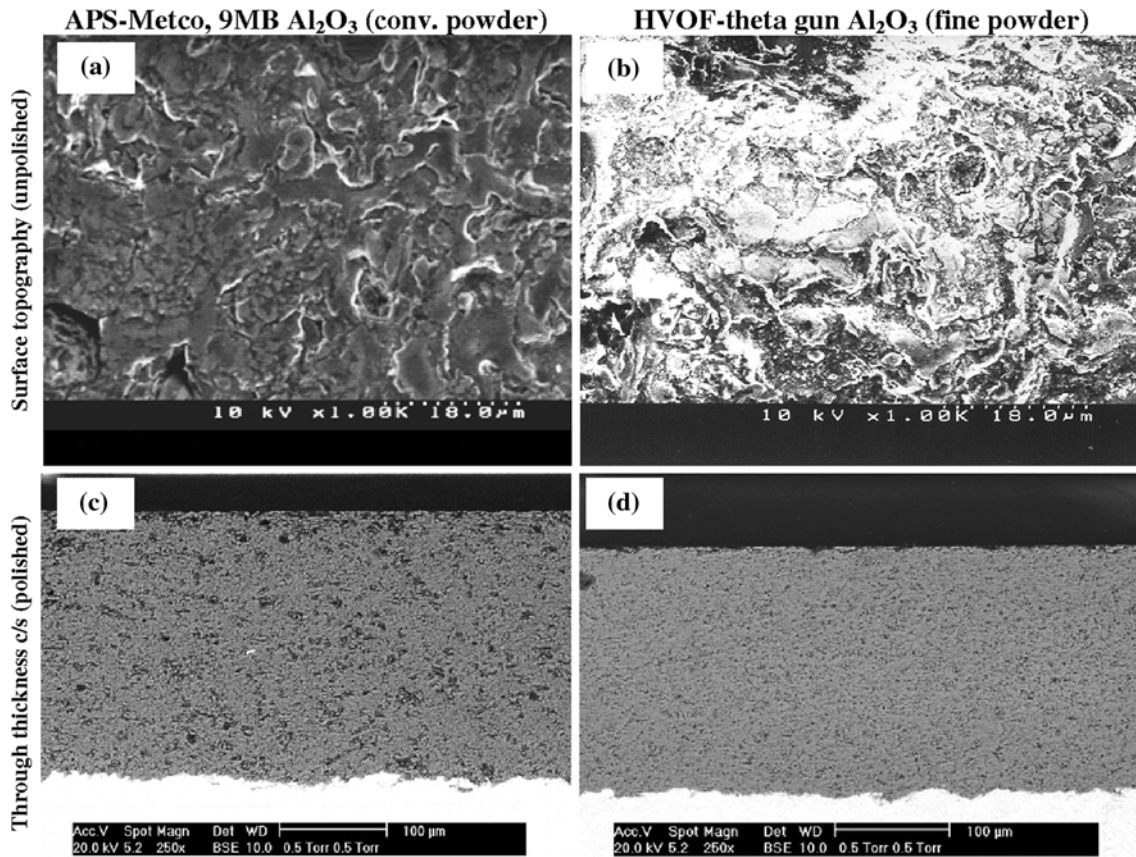
APS-Metco, 9MB Al_2O_3 (conv. powder)   HVOF-theta gun Al_2O_3 (fine powder)

Surface topography (unpolished)

(a)   (b)

10 kV x1.00K 10.0 μm   10 kV x1.00K 10.0 μm

Through thickness c/s (polished)

(c)   (d)

Acc.V Spot Magn Det WD   100 μm   Acc.V Spot Magn Det WD   100 μm
20.0 kV 5.2 250x BSE 10.0 0.5 Torr 0.5 Torr   20.0 kV 5.2 250x BSE 10.0 0.5 Torr 0.5 Torr

Fig. 4 Al_2O_3 coatings: (a) and (b) typical surface topographies exhibiting definite splat morphologies with densely packing splats, (c) and (d) through thickness coating cross sections (polished)

coating and substrate system in this study were 0.64 for APS and 0.69 for HVOF at 100 mN indentation load.

Following the Oliver and Pharr method, the results of the nanoindentation testing are presented in Fig. 5. The hardness, elastic modulus, and maximum indentation depth values quoted are the averaged measurements which were performed on the coating surface, and on four lines distributed along the cross section in the coating and two lines along the cross section in the substrate. The hardness results (Fig. 5a) indicate the upper layers of the HVOF Al_2O_3 coating have higher values than the APS Al_2O_3 coating with little or no effect of the deposition on the stainless steel substrate. The measurements of elastic modulus (Fig. 5b) indicate the upper layers of HVOF Al_2O_3 coating have higher values than the APS Al_2O_3 coating with a higher elastic modulus for APS Al_2O_3-coated stainless steel substrate.

3.3 X-ray Diffraction Analysis

Figure 6(i) shows the XRD spectra of the Al_2O_3 powder and corresponding coating surface. The spectra show the two Al_2O_3 powders to consist of corundum (α-Al_2O_3). The pattern of the APS Al_2O_3 (conventional powder) coating shows it predominantly to contain γ-Al_2O_3 (due to rapid solidification) with some corundum, presumably due

to partial melting of the powder. This is consistent with recent investigations (Ref 35) where the phase content of plasma-sprayed Al_2O_3 coatings at various deposition temperatures indicate a predominantly γ-Al_2O_3 phase. The pattern of the HVOF Al_2O_3 (fine powder) coating shows it predominantly to contain corundum with very little γ-Al_2O_3.

3.4 Neutron Diffraction Measurement of Residual Strain and Stress

A typical neutron diffraction spectrum is shown in Fig. 6(ii), which indicates the diffraction pattern in the coating near the coating-substrate interface. The difference in the range of d_{hkl} spacings recorded between Fig. 6(ii, a) and 6(ii, b) was due to the different chopper settings used to capture the required sections of the diffraction pattern. Figure 7 and 8 shows the residual strain and stress measurements obtained for both coatings, the x axis of which is plotted on a logarithmic scale to highlight the differences in coating strain with depth. Strain results in the APS coating were averaged across the three diffraction peaks of the γ-Al_2O_3 phase (Fig. 6i, b and 6ii, a) which predominantly formed the APS microstructure. The trend of residual strain of all three γ-Al_2O_3 peaks identified in Fig. 6(ii, a) was similar, and hence averaged values
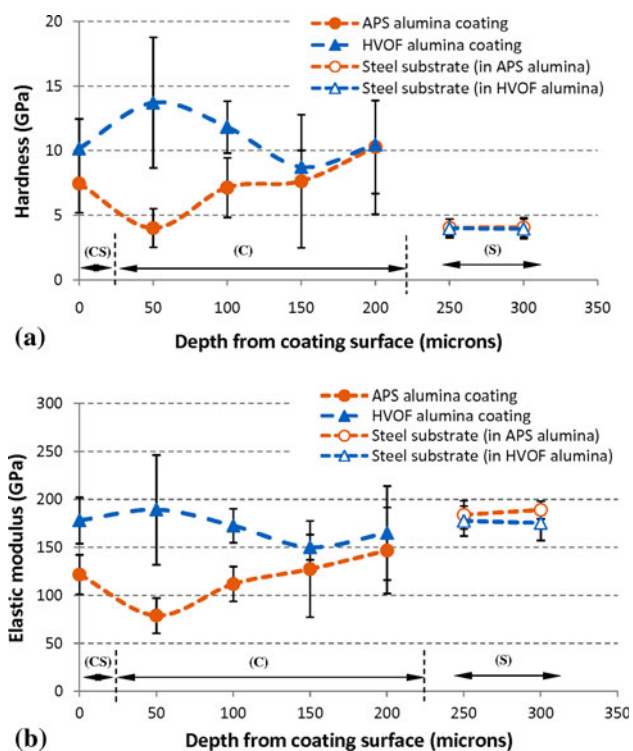
Fig. 5 Nanoindentation results of APS and HVOF (Al_2O_3 coatings and steel substrate) coated specimens: (a) hardness, and (b) elastic modulus (CS: coating surface, C: through thickness coating section, S: substrate section near interface)
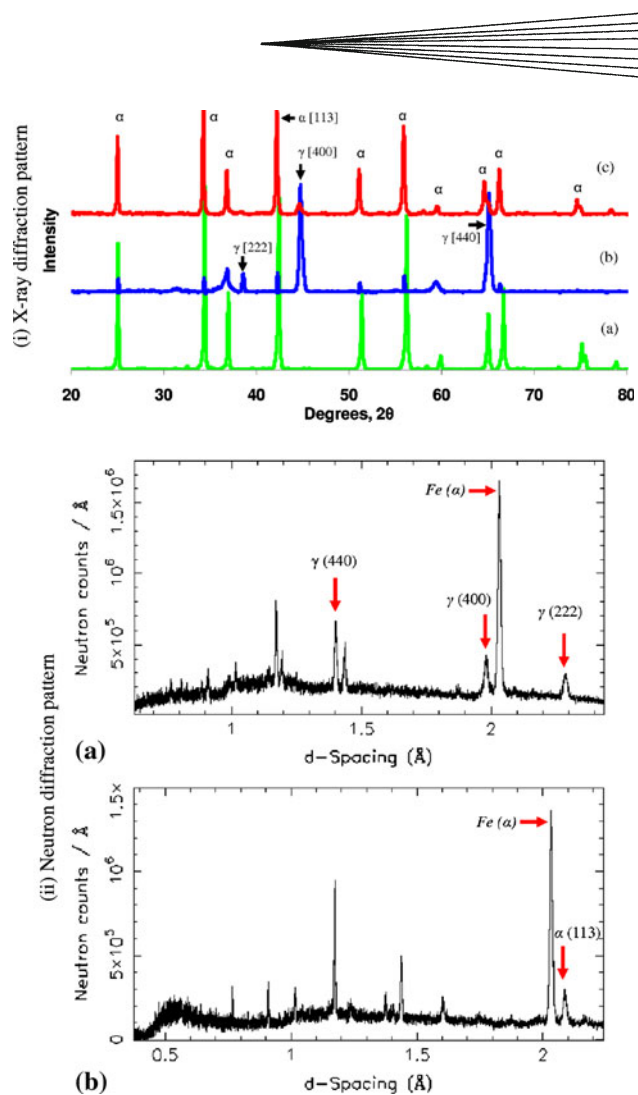

Fig. 6 (i) X-ray diffraction pattern of Al_2O_3 powder (APS) with corresponding deposited coatings: (a) spray powder, (b) APS coating, and (c) HVOF coating. The pattern for HVOF Al_2O_3 powder was similar to APS Al_2O_3 powder as shown in (a), and hence is not presented here; (ii) neutron diffraction pattern near the coating-substrate interface in coating: (a) APS Al_2O_3, (b) HVOF Al_2O_3 (the arrows indicate the peaks identified for and residual strain measurement)

are presented in Fig. 7 and 8. The residual strain in the HVOF coating was measured for the α-Al_2O_3 phase (Fig. 6i, c and 6ii, b) which predominantly formed the HVOF microstructure. These results indicate that the average coating and substrate residual strain and residual stress varied significantly with spraying process and powder size. An average value of elastic modulus (E_s) was used where measurement depth location of residual strain and reduced elastic modulus (E_r) measurement did not match. The residual stress values presented here (Fig. 7b and 8b) were based on approximate Poisson's ratio values of $\nu = 0.231$ for sintered Al_2O_3 and $\nu = 0.30$ for stainless steel.

For measurements at both the center of the specimen (as shown in Fig. 2) at location p_1, and for measurements at a distance 5 mm from the center of the specimen at location p_2, the average residual strain and residual stress, in the HVOF coating changes from tensile to compressive, whereas the average residual strain and residual stress in the APS coating is tensile balanced by a corresponding compressive stress in the substrate. Similar results at both locations (p_1, p_2) indicate that the measured strain behavior using the neutron diffraction technique was reliably indicative of the stress field in the coating/substrate system.

3.5 Vickers Indentation Fracture and AE

Scanning electron microscopic observations of the Vickers indentations and associated raw AE signals of the

Al_2O_3 coatings revealed two different responses, shown in Fig. 9. The indentations of the APS Al_2O_3 (conventional) coatings showed a high degree of crushing fracture and spallation, and the pyramidal impressions were barely discernible in contrast to all the other coated specimens examined (Fig. 9a, column i). Because of the nature of the cracks (meshed and spalled asymmetrically around indentations), it was not possible to measure surface crack lengths either using the direct straight line or profiling method (Ref 22, 23) for the APS Al_2O_3 coatings. In contrast, the HVOF-coated indented samples showed visible radial cracking from all four corners at all loads, and the surface fracture pattern included edge cracks around the indentation (Fig. 9a, column ii).

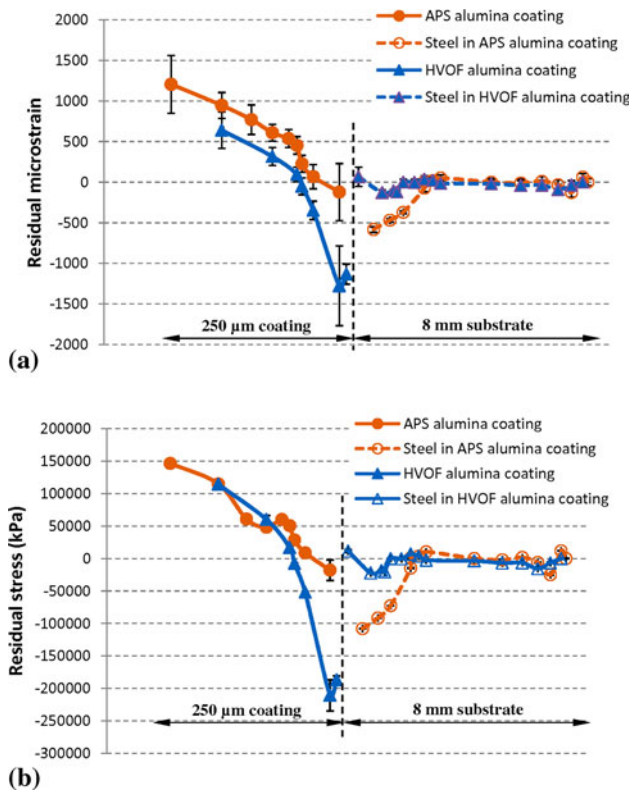Figure 9(b) shows typical time-domain plots for both Al_2O_3 coatings tested (APS and HVOF). The most dis-

Fig. 7 Neutron diffraction for Al_2O_3 coatings at specimen location p_1 (center): (a) residual strain and corresponding (b) residual stress
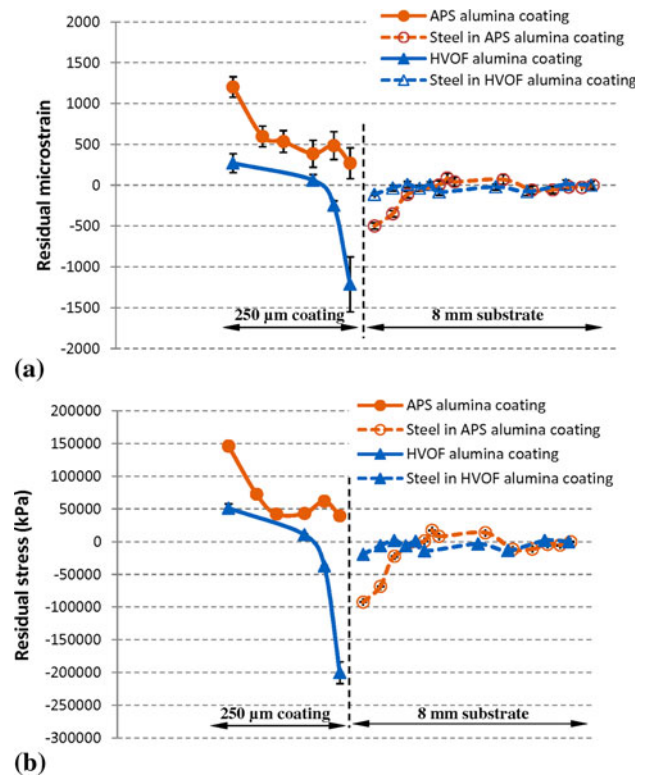

Fig. 8 Neutron diffraction for Al_2O_3 coatings at specimen location p_2 (5 mm offset from center): (a) residual strain and corresponding (b) residual stress

tinct features were a single sharp large peak from the APS Al_2O_3 coatings compared to a lower peak in HVOF Al_2O_3 coatings. These distinct features were used to divide up the AE amplitude-time record into three separate sections (A, B, and C), using the zone sectioning algorithm (Ref 21, 23). The AE-based zone boundaries were identified automatically by first smoothing the absolute raw AE signal using an average of 2000 data points and then applying an automated threshold of 60% below the peak AE amplitude of the total 2 s record, chosen so that its upward crossing identified the zone A-zone B boundary and its downward crossing the zone B-zone C boundary. If there is more than one upward cross and downward cross, then no distinct zones are identifiable. Where three separate zones could be identified, AE features were calculated within each of the AE zones (A, B, and C). Figure 10 shows the numbers of indentations which exhibited clear AE zones, and it is clear that HVOF showed zones for more of the indentations (39 of the 45, i.e., 86%) compared to APS (32 of the 45, i.e., 71%). The frequency-domain showed most of the power to be in the two bands at 100-250 kHz and 300-400 kHz with a minor component discernible between 550 and 650 kHz. Other than this, little was seen to distinguish the spectra.

Figure 11(a) shows total AE features as defined above [e.g., energy (E), event duration (T), and ring-down count (R)] plotted against indentation load for APS Al_2O_3 coatings and, as can be seen, each of these features shows

a rather complex variation with load. It can be observed that the AE energy increases with load until 245 N, followed by a sudden decrease, after which the AE energy broadly remains constant. Figure 11(b) shows total AE features and total surface crack length (L) measured using profiling method (Ref 22, 23) against indentation load for the HVOF Al_2O_3 coatings and, as can be seen, none of the AE features shows a particular pattern with load, although the total surface crack length increases in an approximately linear fashion.

4. Discussion

4.1 Coating Microstructure

The microscopic investigation revealed pores, voids, un-molten particle, nonbonded intersplat areas, and vertical cracks in splats (some distinct features highlighted in Fig. 12). A columnar grain structure was also observed in much of the individual lamellae, which was consistent with previously reported results for plasma-sprayed Al_2O_3 coatings (Ref 5, 10, 35, 36). The columnar structure occurs as the crystallization of lamella occurs in strongly non-equilibrium conditions and the molten material loses heat mainly by conduction to the underlying material in a direction perpendicular to the plane of the underlying material, as indicated previously by Forcey and Iordanova
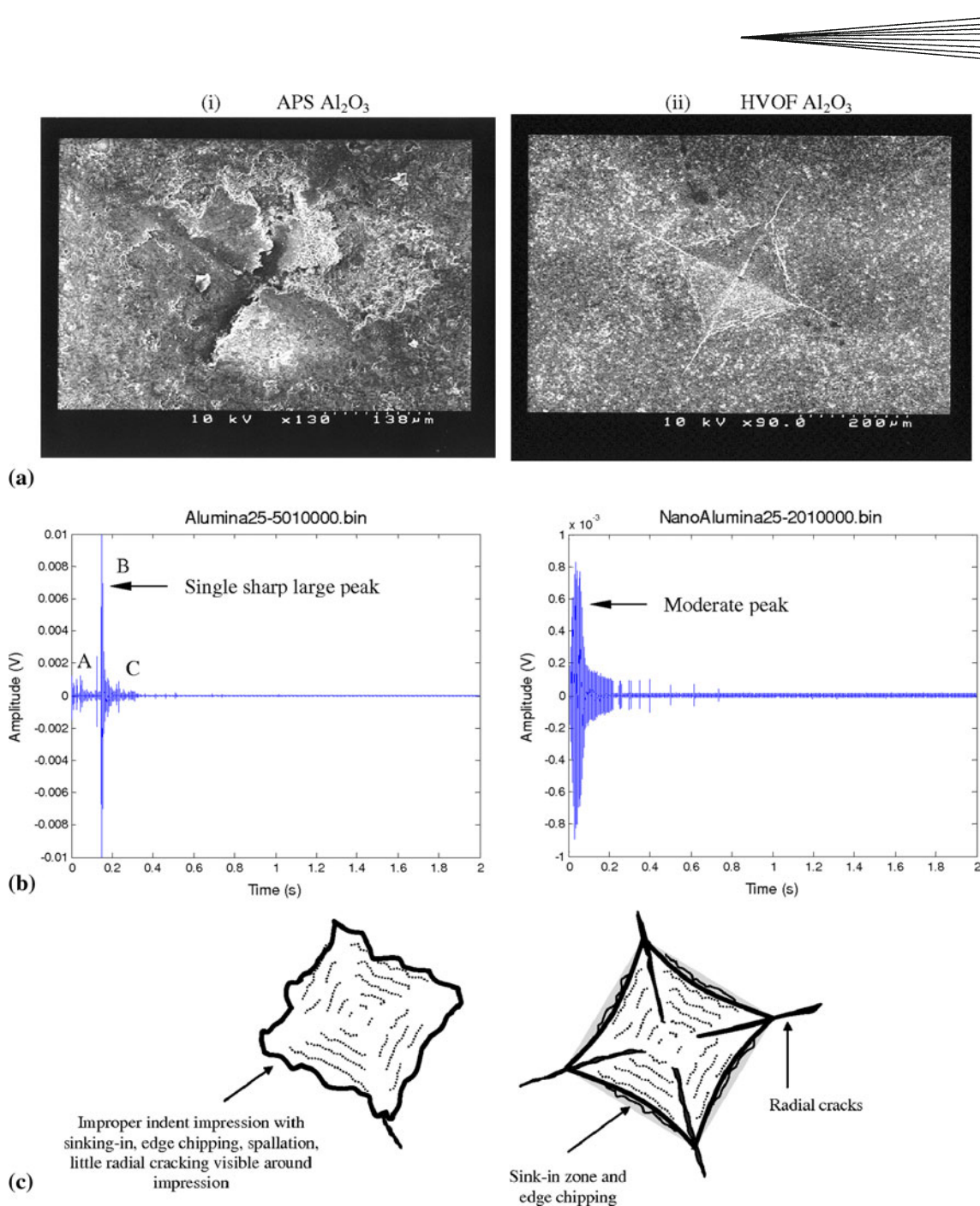
Fig. 9 Vickers indentation at 245 N load of Al_2O_3 coatings: (a) typical cracking patterns of coating surface and (b) corresponding amplitude-time AE signal structure (A, B, and C represents three distinct AE zones shown for APS Al_2O_3 coatings, note the 10 times lower magnitude (y axis) for HVOF Al_2O_3), and (c) schematic of typical Vickers indentation residual impressions

(Ref 37). They proposed that the crystallization will start from a base layer within the splat and proceed rapidly in the opposite direction to the heat flow, i.e., from base of the splat to the top surface, giving a fiber texture (columnar structure). A more recent study which considered the fiber and texture direction within the splats by Shinoda et al. (Ref 38) has indicated that for YSZ coatings, the conventional expectation of columnar structure growing in a plane of heat extraction, i.e., which had orientation perpendicular to the substrate, cannot fully

explain the discordance between the column growth and fiber axis in splat formation. Hence, although the heat extraction direction is generally responsible for a columnar texture, other factors especially in ceramics such as YSZ e.g., preferred crystallographic orientations (microtexturing) within splats also play a dominant role.

The splat thickness appears to be similar in the two coatings despite the very different powder sizes (1-5 μm for HVOF and 10-45 μm for APS Al_2O_3), but the splats appear more lamellar but less cohesive (layer gaps
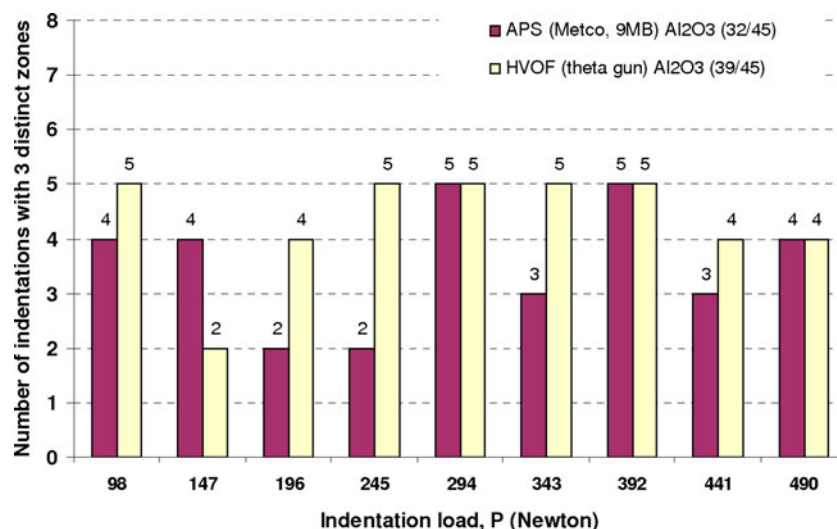
Fig. 10 Number of indentations with distinct AE zones A, B, and C

between splats) in the APS coatings. Similarly un-molten particles feature in the microstructure of the HVOF coating, which is consistent with the relatively low heat input and higher particle velocity of HVOF (Ref 39).

4.2 Coating Morphology

The XRD analysis of the two Al_2O_3 powders indicated no difference between them, both being predominantly α-Al_2O_3. The XRD showed that the APS Al_2O_3 (conventional powder) coating consisted mostly cubic γ-Al_2O_3 (due to rapid solidification) with some hexagonal α-Al_2O_3 in the coating, mainly residue from unmolten or partially molten spray powder (Ref 5, 10). The XRD pattern of the HVOF Al_2O_3 (fine powder) coating shows it predominantly to contain α-Al_2O_3 with little γ-Al_2O_3 indicating very limited phase transformation for this coating process.

For plasma-sprayed Al_2O_3 coatings, Mušálek et al. (Ref 36) investigated the splat morphologies, with a view to understanding the zones of subsurface stress concentrators, e.g., pores, vertical cracks in splats or oxides; whereas, Hao et al. (Ref 35) investigated the microstructure and properties of plasma-sprayed Al_2O_3 coatings which were significantly influenced by the deposition temperature. As was seen in Fig. 12(a), the constraining of splats led to the formation of submicroscopic fragmentation or vertical cracks of splats and their coalescence resulted in typical brittle failure for APS Al_2O_3. The HVOF Al_2O_3 (Fig. 12b) coating appears to have fewer gaps or voids between splats, indicating relatively higher bond strength.

4.3 Nanohardness and Elastic Modulus

The nanohardness results (Fig. 5a) suggest that the spraying conditions using APS and HVOF techniques produced little or no effect on the hardness of the substrate, whereas the upper layers of the HVOF coating had a higher average value than the APS coating. This difference in the

average hardness can be attributed to the considerably lower degree of phase transformation in the HVOF coatings (Fig. 6). This could also lead to potential differences between the measured elastic values. However, other factors such as intersplat bonding (cohesive strength), residual stress and porosity also contributed to the differences in the elastic modulus of two coatings. This is consistent with investigations in other materials, where the applied stress has been shown to alter the hardness of materials (Ref 40).

The measurements of elastic modulus (Fig. 5b) suggest that the top layers of HVOF Al_2O_3 coating had a higher elastic modulus than APS Al_2O_3 coating. High standard deviations in through thickness nanoindentation measurements (hardness, elastic modulus, and maximum indentation depth, Fig. 5) also suggest a significant effect of the complex coating morphology. The elastic modulus results of the substrate, near the coating-substrate interface, suggest that the spraying conditions using APS had a slight increase in the average modulus values compared to HVOF techniques, although the average (APS/steel substrate: 186 ± 12 GPa, HVOF/steel substrate: 176 ± 16 GPa) of both coating substrates is still within the standard deviation. The effect of deposition condition on the average substrate modulus possibly arose due to the higher deposition temperature during APS spraying. High magnification images of etched-steel substrate near the interface indicated negligible differences in the microstructure of both steel substrates. Also, the hardness did not show significant differences between the near-interface hardness of the steel substrate between the two coating processes, indicating that carbide and microstructural transformation was not significant, which will be consistent with the observed microstructure. Hence, it is difficult to relate this change in modulus of near-interface modulus of steel on possible microstructural transformations in steel during coating deposition. It is therefore postulated that the higher apparent modulus of steel near the coating-substrate interface in APS coating was caused
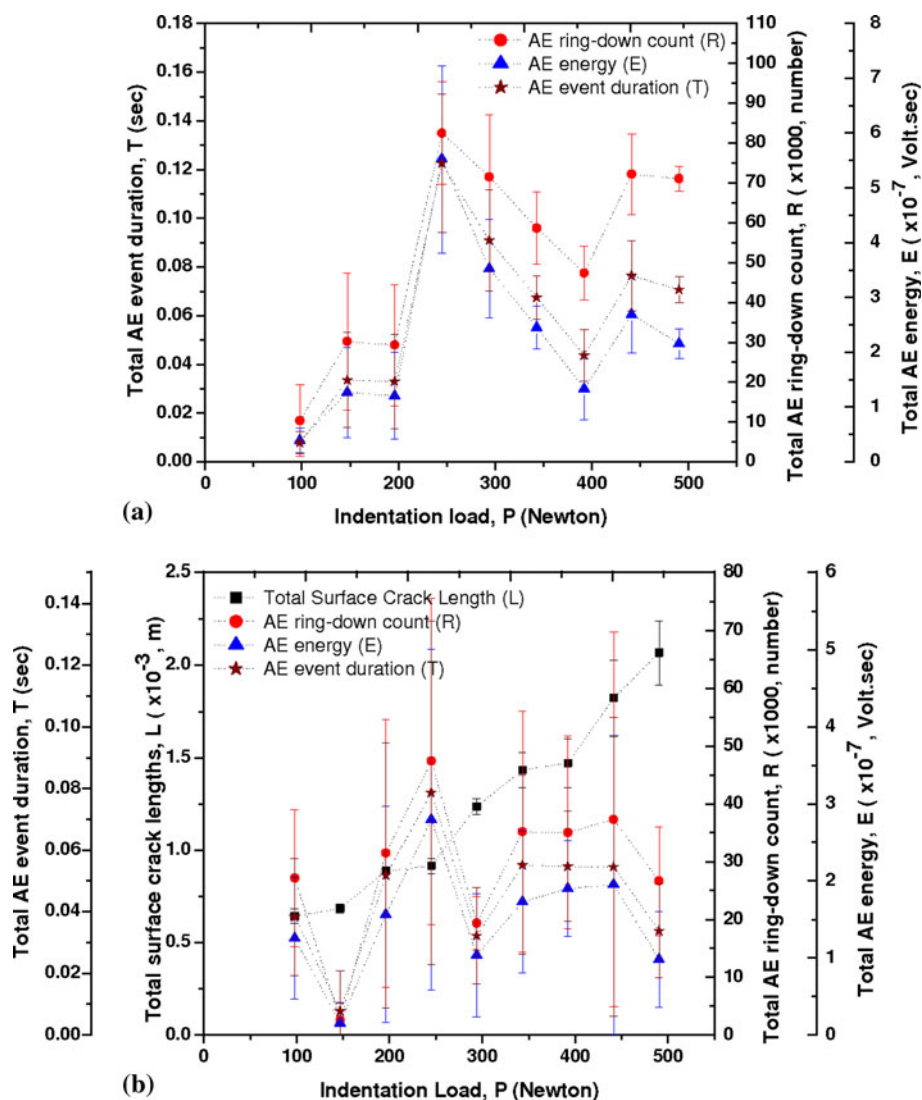
Fig. 11 Effect of indentation load on AE features (a) APS Al_2O_3 coatings, and (b) HVOF Al_2O_3 coatings, including total surface crack length

by the largely compressive residual stress in the steel substrate (Fig. 7 and 8). Other investigations (Ref 40) have indicated that elastic modulus measurement can be influenced by residual stress, which can be attributed to the differences in the real and measured indentation contact areas. Hence, as the hardness is calculated based on the area of contact and modulus slope of the unloading curve, they do not follow similar trends in the near-interface substrate region.

Nanoindentation modulus measurements were used for the transformation of residual strain to stress as they reflect the dependency of the modulus on the coating microstructure. The dependency of diffraction modulus on one of the microstructural features (porosity) in plasma-sprayed coatings was previously investigated by Gnaeupel-Herold et al. (Ref 41) for IN625 coatings. They indicated in their work that as the porosity level increased with the coarsening of powder particles, the diffraction modulus decreased. In this study, the porosity was

measured as 2.8 ± 0.64 and 8.8 ± 2.0 for the HVOF and APS coatings, respectively. Indentation modulus measurements (Fig. 5b) indicate this dependency on porosity among other microstructural features. At the load of 100 mN, the Berkovich indentation (approximately 8.4 μm impression diagonal) was landing on 3-4 splats (typically splat thickness was ~1-2 μm) indicating that any porosity between splats would have an effect on the modulus measurement. Even if a constant nonporous bulk value of diffraction modulus were used, although it would change the absolute values of stress, the relative difference between the stress measurements between the two coating layers will remain the same as that of the strain differences (Fig. 7a and 8a).

4.4 Coating Residual Strain and Stress Profile

As was seen in Fig. 7 and 8, the residual strain and stress profiles in the HVOF Al_2O_3 coating changed from
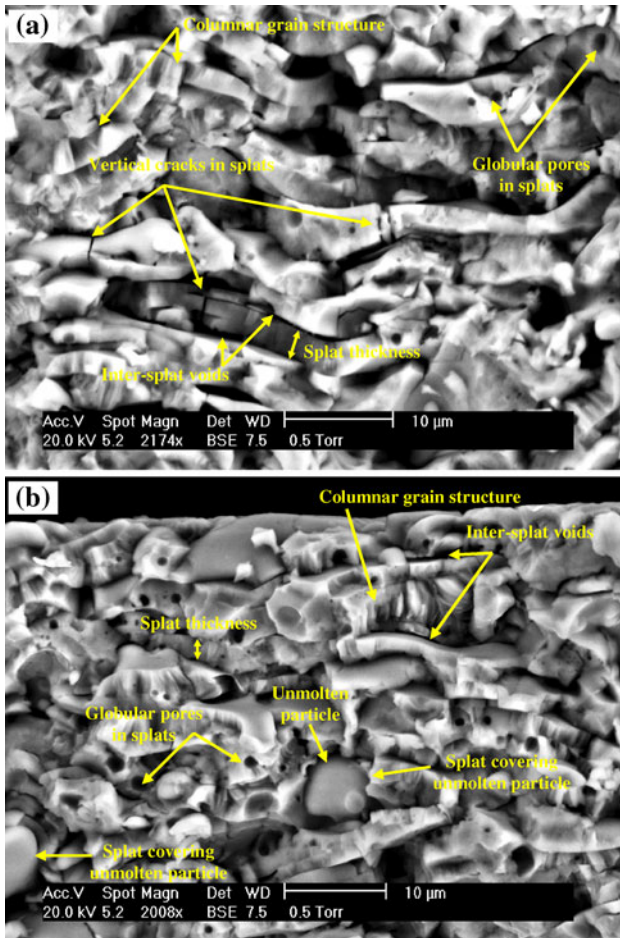
Fig. 12 Back-scattered ESEM images of cryogenically fractured coatings showing the Al_2O_3 coatings exhibiting definite splat morphologies with columnar grain structure, revealing splats, pores, voids, vertical cracks in splats and unmolten particles: (a) APS Al_2O_3 and (b) HVOF Al_2O_3

equation for the evaluation of this residual stress (σ) component using Eq 5 (Ref 2, 44):

$$\sigma_{c,s} = E_{c,s}\left(\frac{x}{l} - \alpha_{CTEc,s}\Delta T\right) \qquad (Eq\ 5)$$

where* $E_{c,s}$ and α_{CTE} represent the elastic modulus and CTE of the coating layer and substrate materials. The term x/l represents the net strain due to constrained contraction and ΔT represents the temperature change. For the case of APS Al_2O_3 and HVOF Al_2O_3 coatings considered in this investigation, although the material properties considered in the above equation can be considered similar for both coatings, ΔT will be higher for the APS coatings due to its higher deposition temperature in comparison to the HVOF coating (Ref 39). This will lead to higher macro-compressive stress in the APS coating as** $\alpha_{CTEc} < \alpha_{CTEs}$ (Ref 45). The residual stress in HVOF coatings was predominantly compressive, which is consistent with Eq 5. Measured values of residual stress in APS coatings (Fig. 7 and 8), and also reported values of residual stress measurement in the published literature (Table 2) in Al_2O_3 coatings, however, indicate a tensile residual stress, and this is supported by the observations of microcracking. This is inconsistent with this predicted strain behavior on the basis of CTE and deposition temperature differences (Eq 5).

4.4.2 The Role of Quenching Stress. The quenching stresses, which appear within individual splats, are caused by the constrained contraction of the solidifying splat as it cools, since its contraction is constrained by the underlying lamella or material. This again is a function of temperature of individual splats and also size of powder particles. As stipulated above, the deposition and hence the lamella temperature will be higher in the APS coatings, which will lead to higher average quenching stress. This will result in a higher value of quenching residual stress (tensile) in the APS coatings. The smaller size of powder particle in HVOF coatings will increase the density of interstrat boundaries and hence result in quenching stress relaxation, on the assumption that there will be less straining due to a lower constraining contact area between individual splats (as splat diameter will be lower in HVOF), and also less constraint between neighboring splats due to increased splat boundary density. Another mechanism of stress generation which relates to the pore morphology indicates that the decrease in powder particle size increases the residual stress in thermal spray deposits (Ref 8, 9). This effect is attributed to the higher surface area to particle volume ratio of smaller particles, resulting in changes in the pore and interstrat morphology, which resists stress relaxation in the deposited layer. In the investigation by Coats and Krawitz (Ref 8) on WC-Co coatings, it was concluded that with the increase in powder particle size the tensile stress in the Co and the

tensile to compressive, whereas in the APS Al_2O_3 coating the residual stress is largely tensile. These values illustrate the combined effect of phase transformations, thermal mismatch, peening effect, quenching of lamellae and difference in the coefficient of thermal expansion (α_{CTE}) of the coating/substrate system (Ref 1-5, 10-12, 14-17).

On the basis of physical mechanisms dictating the residual strain behavior, there are four major factors which contribute to the through thickness residual strain profile in these coatings. These factors, based on the differences in the coating deposition temperatures, velocity and size of coatings particles between the APS and HVOF coatings are discussed below:

4.4.1 The Role of Deposition Temperature. Macro-residual stress occurs due to the differences in the CTE of coating and substrate materials. Different approaches have been adapted in the published literature to model the influence of this mechanism of strain generation, which vary from the bending Almen test (Ref 42) to mathematical (Ref 2) and numerical models (Ref 13, 43). A simplified mathematical approach uses the mathematical

---

*Subscripts c and s relate to the materials properties for the coating layer and substrate, respectively.

**α_{CTE} of Al_2O_3 (7.10×10^{-6} °C^{-1} to 10.5×10^{-6} °C^{-1} at temperatures of 127-1327 °C, respectively (Ref 46) and 440-C steel (average value of 11.2×10^{-6} °C^{-1} in the temperature range of 20-600 °C (Ref 46).

Table 2 Literature results of residual stress in thermally sprayed Al_2O_3 coatings

Residual stress measurement method	Coating process	Al_2O_3 coating thickness, µm	Elastic modulus of Al_2O_3 coating (E_c, GPa), measurement method	Al_2O_3 crystal plane (hkl)	Substrate details	Residual stress in Al_2O_3 coating (σ_R, MPa) +ve: tensile −ve: compressive	Comments on residual stress profile	References
Neutron diffraction	APS	2000	250	400, 440	Steel, 2.5 mm	0 to −100	Through thickness compressive profile and tensile toward the surface	Ref 16
	APS	2160	200	430	Fe	−100 to +100	Through thickness compressive to tensile toward the interface	Ref 17
X-ray diffraction	APS	400	70	...	Hot rolled steel Fe37	+82.5	Tensile surface	Ref 10
	APS	220	300	844	St 37 K steel, 2 mm	+410 ± 60	Tensile surface	Ref 11
	APS	150	87		Steel AISI 1040	+220	Tensile surface	Ref 12
	APS	1200	343	214	Steel	+420 ± 36	Tensile surface	Ref 14
			360			+431 ± 24	Tensile surface	
	HVOF	210	300	844	St 37 K steel, 2 mm	+190 ± 25	Tensile surface	Ref 11
	HVOF	150	138	...	Steel AISI 1040	+116.5	Tensile surface	Ref 12
	HVOF	150	138	...	Steel AISI 1040	+136.5	Tensile surface	Ref 12
	APS	350	45 (four-point bending test)	...	Low C steel, 4 mm	+260 ± 40	Through thickness random variation, Tensile surface	Ref 15
Hole drilling	APS	400	70	...	Hot rolled steel Fe37	0 to +80	Through random thickness variation, tensile surface	Ref 10
	APS	1200	...	...	Steel	+400 to −400	Through thickness random variation, tensile and compressive	Ref 14
	APS	320	...	...	Steel AISI 4037	−30 to −50	Through thickness compressive variation	Ref 13
Finite element method	APS	320	...	...	Steel AISI 4037	−55 to −65	Through thickness compressive variation	Ref 13

compressive stress in the WC decreased. However, these investigations (Ref 8, 9) related to the influence of powder size on the residual stress were conducted for a given coating process and hence do not provide a direct comparison for the current investigation, as the coating method and powder size were different.

4.4.3 $\alpha \rightarrow \gamma$ Phase Transformation. As indicated in Fig. 6(i), there was a higher degree of $\alpha \rightarrow \gamma$ phase transformation in the APS coatings. As indicated in previous literature (Ref 10), the density of α-Al$_2$O$_3$ is higher in comparison to γ-Al$_2$O$_3$. This means that there is a small volume increase in the $\alpha \rightarrow \gamma$ phase transformation (crystal structure for α-Al$_2$O$_3$: hexagonal, crystal structure for γ-Al$_2$O$_3$: cubic) (Ref 10). This increase in volume will provide a relaxation mechanism at intersplat boundaries for the APS coatings, leading to lower residual tensile strain. However, based on the measured values of tensile residual strain, this indicates that the contribution of residual strain from this phase transformation was less significant than the deposition temperature and quenching stress discussed above.

4.4.4 Peening Effect. The peening effect in the HVOF process, due to the relatively high particle velocity, is understood to cause compressive residual stress in thermal spray coatings. A simple calculation of kinetic energy per unit area of splat for the two coating powders and processes indicate that for a typical (Ref 39) average particle velocity of 300 ms^{-1} for 45 μm APS powder, and 800 ms^{-1} for the 5 μm HVOF powder, the kinetic energy per unit area of splat (assuming splat thickness of approximately 2 μm for the APS and 1.5 μm for the HVOF splat) as observed in SEM images (Fig. 12) will be almost an order of magnitude higher in the HVOF process. This, coupled with the higher hardness of the HVOF powder particles at the time of impact due to its lower temperature, as observed by the un-molten particles, will further increase the peening effect and impart higher compressive residual stress on the underlying layers in the HVOF coatings. In the current investigation, a similar trend can be observed for the compressive residual strain in the HVOF coating.

4.5 Vickers Indentation Behavior and Residual Stress

This section is confined to discussing indentation accommodation behavior, fracture toughness, motivation for AE-based indentation fracture monitoring, and the effect of preexisting residual stress on coating failure during indentation.

4.5.1 Indentation Behavior. Two different cracking patterns around indentations can be seen in Fig. 9(a) for both Al$_2$O$_3$ coatings. In the thermally sprayed ceramic/cermet coating materials, indentation accommodation is by crumbling of the surface (based on a "sinking-in" mechanism) to the extent that cracking cannot be entirely quantified by metallographic means (Ref 21-23). Cracks within elastic stress field [Boussinesq field (Ref 47)] can initiate from preexisting flaws (Ref 48) or flaws induced by the indentation itself (Ref 47). On attaining some critical configuration, a dominant flaw develops into a well-defined propagating crack, and tends to propagate along trajectories which maintain near orthogonality to a major component of tension in the Boussinesq field.

Using the finite element method, Baung et al. (Ref 49) simulated Vickers indentation behavior on HVOF WC-Co coatings to determine the indentation stress distributions and critical loads, relating their findings to the observed cracking profile around the indentation. The finite element simulation indicated that the highest compressive stress occurs in the area right beneath the indenter tip and the highest tensile stress occurs in the center of the indentation edges and decreases along the indentation edge toward the indentation corner. This suggests that edge cracks will initiate first at the coating surface, and will propagate along the indentation edge. Also, the high tensile stress in the area of the indentation corners induces corner cracks to propagate radially outward along the diagonal of the indentation. Therefore, edge and corner cracks in Fig. 9(a, ii) for HVOF Al$_2$O$_3$ coatings can be explained based on the above discussion.

Stoica et al. (Ref 50) used the fracture pattern around Vickers indentations in functionally graded HVOF WC-NiCrBSi coating surfaces to make a qualitative assessment of fracture toughness because these coatings did not meet the empirical model criteria (Ref 51) ($c > 2a$). The empirical models tend to be based on an idealized cracking pattern and do not account for microfissuring in the subsurface region, especially if this takes the place of surface-radial cracks as it does at lower loads. The uncertainty in measuring the crack lengths in Vickers indentation makes empirical models particularly unsuitable for thermal sprayed coatings (Ref 52). Irregular networks of smaller cracks not originating at indentation corners have been observed by other investigators (Ref 50, 52-54) working on thermally sprayed coatings. For example, Ostojic and McPherson (Ref 54) reported "no dominant cracks" in plasma-sprayed Al$_2$O$_3$ coatings even very close to the impression. The indentation fracture in these coatings also tends to be asymmetric, which has been attributed by Ostojic and McPherson (Ref 54) to a macroscopic variation in relative density, the presence of pores or other defects around the contact and through thickness residual stresses variation. It has been suggested (Ref 54) that indentation in porous regions of the coatings results in localized densification about the contact site, resulting in little transmission of indentation stresses to the surrounding materials, and the confinement of cracking to the vicinity of the impression. Interaction with large coating pores or defects near the impression diagonal would then be expected to result in longer cracks, producing a modified (Boussinesq) stress field. Comparison of Fig. 9(a) (column i and ii) indicates that modification of Boussinesq stress field is more dominant in APS than HVOF Al$_2$O$_3$ coatings. Since the degree of porosity varies between coatings (Fig. 4c and 4d) as well as within a given coating, Ostojic and McPherson (Ref 54) also suggested that different loads would be required to produce cracking in different coatings of the same type and even from place to place in a single coating.

4.5.2 Indentation Fracture Toughness. Based on typical microscopic images shown in Fig. 9(a), and as schematically categorized in Fig. 9(c), the Vickers indentations of the coatings fracture differently and it is by no means certain that the classical approach (either Palmqvist or Half-penny crack models) (Ref 51) of using radial crack length to deduce fracture toughness measurement will be valid when some (or all) of the cracking is distributed in relatively short edge cracks (Ref 21-24). From the present Vickers indentation fracture observation, it seems reasonable that coatings fracture differently, because APS Al$_2$O$_3$ coatings usually consists of γ-Al$_2$O$_3$ (Fig. 6i, b) with relatively similar splat morphology (Fig. 12) and will give a low mechanical performance compared with HVOF Al$_2$O$_3$ coatings which usually have α-Al$_2$O$_3$, because the mechanical performance of γ-Al$_2$O$_3$ is lower compared with that of α-Al$_2$O$_3$ (Ref 10). Using the classical crack régimes in Vickers indentation fracture tests, the average crack-to-indent ratio (measured l_a/a about 0.88 ± 0.21 for HVOF-θ-gun Al$_2$O$_3$ fine powder), suggests Palmqvist rather than median cracks. Assuming the Palmqvist model, the fracture toughness for the HVOF-θ-gun Al$_2$O$_3$ (fine powder) coatings studied here was 5.5 ± 0.5 MPa m$^{1/2}$. For a similar coating material (HVOF Al$_2$O$_3$, powder size unknown), Bolelli et al. (Ref 12) have given a value of 2.5 ± 0.57 MPa m$^{1/2}$, although they did not indicate the direction of indentation and what fracture model they used. For APS (Metco 9MB) Al$_2$O$_3$ (conventional powder) coating, where a measurement of K_{1c} was not possible in this study, Bolelli et al. (Ref 12) have given a value of 2.33 ± 0.36 MPa m$^{1/2}$, although, again, powder size, indentation direction, and fracture model were not specified.

4.5.3 AE-Based Indentation Fracture Monitoring. As cracking becomes more distributed into smaller and smaller units, measurement of total crack length rapidly becomes impractical, offering a motivation for AE-based indentation crack monitoring. The uncertainty in quantifying and measuring the total cracking surface in indentation makes a simple fracture-mechanics-based assessment of toughness difficult for all but the simplest cracking patterns. It is therefore expected that correlation between AE and fracture patterns will lead to an improved method for material quality evaluation. As was seen in Fig. 11, at most of the indentation loads (6 out of 9) the AE energy for APS Al$_2$O$_3$ coatings is higher than that for HVOF Al$_2$O$_3$ coatings, which is due to the combined effect of microstructural morphology, low fracture toughness and residual tensile stress. The AE-based analysis suggests that total AE energy can make a useful proxy measure for total crack area for material of a given fracture toughness and elastic modulus (Ref 21-24).

For the cases where cracking can be measured (in HVOF Al$_2$O$_3$ coatings, Fig. 11b), it appears that zoning is associated with a large total crack length and the appearance of radial cracks. The fact that AE zoning also appears in another sample (in APS Al$_2$O$_3$ coatings) where the crack length could not be measured suggests that it is the presence of a significant amount of cracking that leads to the zoning of the AE. This is consistent with cracking

being a discontinuous accommodation process, unlike plastic deformation which is more continuous, and is also consistent with the literature on homogeneous materials (Ref 55-57) where the radial cracking is seen to be discontinuous and that it leads to burst-type AE at particular critical loads.

Of the records that exhibited AE zoning, Fig. 13 shows that zone A always represents a small proportion of the total AE energy (also of the other measures, ring-down count and event duration), and that zone C contained the most energy at moderate to higher loads. The fact that zone C shows the biggest change with load would suggest that cracking during indentation is better discriminated using zone C, although zone B often contains the highest intensity of cracking events. The zoning of AE signals, and the associated energy (Fig. 13) might be useful in understanding the evolution and nature of cracking events but the fact that it has not been observed in all records examined makes it difficult to form general conclusions.

Supposing that crack depths are approximately constant, AE could then be considered to give a measure of total surface crack length, so that the Eq 4 can be modified
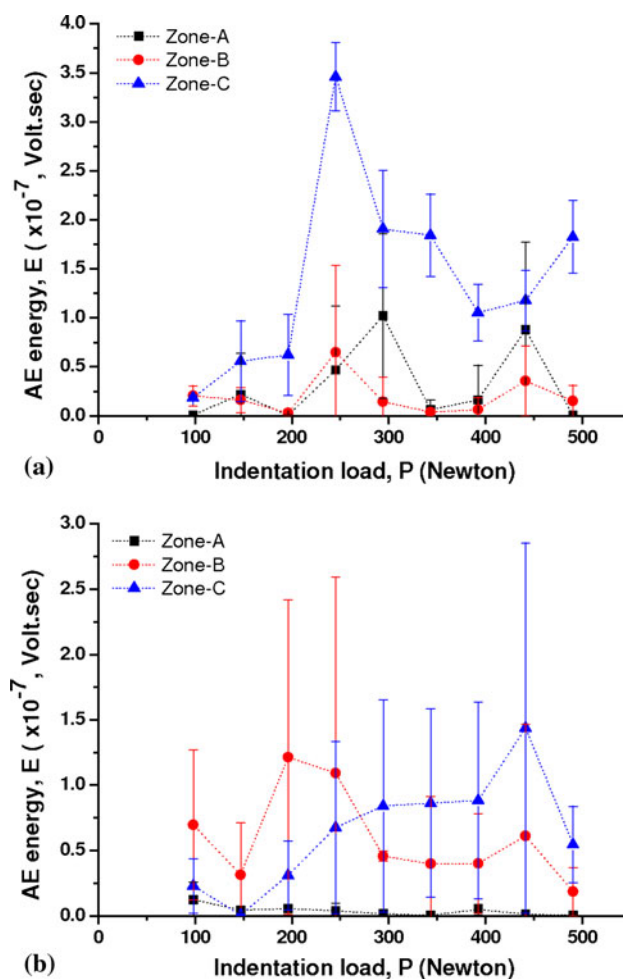

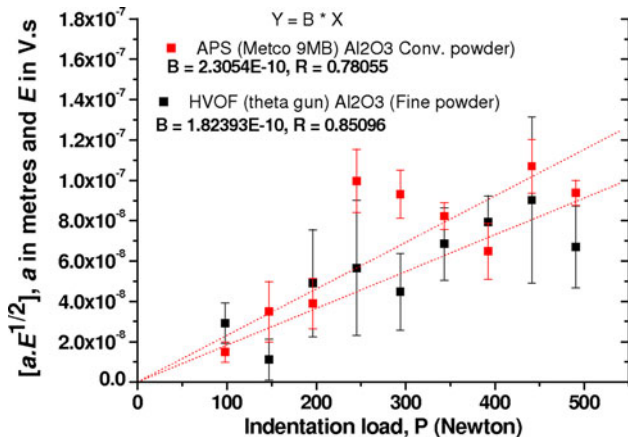**Fig. 13** Zone AE energy: (a) APS Al$_2$O$_3$ coatings and (b) HVOF Al$_2$O$_3$ coatings

Fig. 14 AE-based (using modified generic equation) indentation fracture toughness estimation using AE energy (E) for APS and HVOF Al_2O_3 coatings (lower the slope of best-fit line, higher the fracture toughness)

(Ref 22, 23) to $K_{1c} = k_{AE}\left[\frac{P}{a\sqrt{E}}\right]$, where k_{AE} is an AE-based empirical constant which can, in principle, be determined for any indenter-specimen-AE system combination. Figure 14 shows plots of $a\sqrt{E}$ against P along with the associated best-fit straight lines and the values of the slopes (lower the slope of best-fit line, higher the fracture toughness, e.g., for HVOF Al_2O_3 coatings) and their correlation coefficients alongside the corresponding values for the AE energy. The fact that these correlations are reasonably good indicates that the AE approach can be calibrated against the crack length-based assessment to allow an assessment of the toughness for the materials, where an AE record is available and crack length could not be measured (Ref 23).

4.5.4 Combined Effect of Indentation Stress and Preexisting Residual Stress on Coating Failure. Apart from the elastic stress field (Boussinesq field) due to indentation, a preexisting residual stress field in a material can strongly affect mechanical performance (such as fatigue strength, delamination, fracture toughness, and wear resistance) which influences the reliability and lifetime of components (Ref 58). There is no simple relationship between cracking pattern and total stress distribution during indentation, but combined indentation stress (σ_I) and preexisting residual stress (σ_R) can affect the indentation response of materials significantly (Ref 58, 59). However, using the ''same load indentation'' approach (Ref 60), a preexisting residual tensile stress (Fig. 7 and 8, preexisting residual tensile stress higher for APS Al_2O_3 coating) at the surface is expected to facilitate the penetration of the indenter, whereas a preexisting residual compressive stress is expected to reduce the penetration of the indenter.

The combined effect of indentation stress and preexisting residual stress in thick hard coatings have been investigated by Chen et al. (Ref 59) using the finite element, method where it was suggested that the indentation compressive stress diminishes with preexisting residual

tensile stress, which leads to an enlarged plastic zone and gives apparent high penetration. Whereas, with a preexisting residual compressive stress the maximum indentation compressive stress is increased, causing less plastic deformation and giving rise to lower penetration. Since indentation pressure is compressive just below the indenter tip and perpendicular to the applied surface, the existence of tensile residual stress (relatively higher for APS Al_2O_3 coating, Fig. 7 and 8) in the surface will increase the magnitude of shear stress leading to surface failure beneath the indenter as was seen in the form of localized mesh and spallation (Ref 53, 54) for APS Al_2O_3 coating (Fig. 9a, i). However, relatively less preexisting tensile residual stress in the surface for HVOF Al_2O_3 coating reduced the coating failure in the form of localized mesh and spallation, dominating the effect of indentation stress field (Boussinesq field) failure, as was seen in the form of typical corner radial and edge cracking (Ref 21-24, 31-33, 47, 51, 58) (Fig. 9a, ii).

It is also known that a through thickness preexisting residual stress profile plays a very important role in the extension or suppression of cracking (Ref 2, 3): for example, it has been observed that at the same Vickers indentation load, the relatively high preexisting residual compressive stresses measured by neutron diffraction in HIPed WC-NiCrBSi coatings (Ref 2) inhibited the extension of cracks seen in the as-sprayed coating (Ref 50). Considering the existence of preexisting tensile residual stress (in upper layers) for the APS Al_2O_3 coating (Fig. 7 and 8), Vickers indentation is expected to induce significant and large cracking and therefore relatively high AE energy (Fig. 9b, ii and 11). It is also known that porosity plays an important role in thermally sprayed coatings fracture during indentation (Ref 24). To characterize the effect of porosity in plasma- and flame-sprayed Al_2O_3 coatings Safai et al. (Ref 19) used an AE feature (event count) and suggested that the amount of cracking due to porosity in the plasma-sprayed coatings can be approximately one-half that of the flame-sprayed coatings, and suggested that a reduction in AE event count can be representative of reduced porosity. Considering the differences in the porosity (2.8 ± 0.64 and 8.8 ± 2.0 for the HVOF and APS coatings, respectively), Vickers indentation is expected to induce significant and large cracking and therefore relatively high AE energy for APS coatings.

Comparing the microstructure morphology, phase composition, neutron diffraction residual stress profile and AE energy, and from the present Vickers indentation fracture observation, it seems reasonable that APS Al_2O_3 coatings will give a low mechanical performance compared with HVOF Al_2O_3 coatings. Among other methods (Ref 61), one of the methods used to estimate residual stress in brittle materials is indentation cracking (typically performed for estimating indentation fracture toughness) (Ref 60). A recent review (Ref 24) concludes that a number of investigations examine the critical load of cracking using AE during indentation, and therefore there is scope for residual stress measurement with proper calibration. However, the indentation technique
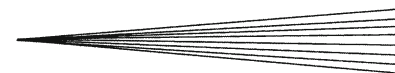
of residual stress measurement cannot be applied to a material showing a strong dependency of the residual stress on its direction (anisotropic materials, e.g., coating/substrate system) as the indenters basically give an average response of the near surface residual stress state only.

5. Conclusions

For the two different thermal spray deposition techniques, process parameters and powder sizes explored in this study, a combined approach using liquid nitrogen freeze fractographic analysis, neutron diffraction residual strain measurement, and AE-based Vickers indentation fracture monitoring has been demonstrated. The following conclusions can be drawn:

- It is concluded that the through thickness residual stress profile in the APS Al_2O_3 coating was mainly tensile, being lowest at the interface with the substrate whereas the HVOF Al_2O_3 coating had a compressive tensile residual stress at the interface which becomes tensile approaching the coating surface.

- Four factors contributed to the differences in the residual strain behavior of the APS and HVOF coatings: lamella temperature, particle velocity, particle size, and microstructural differences. Among them, the effect of particle size was quantitatively specified whereas the other factors of lamella temperature and velocity were qualitatively compared.

- The microstructural differences along with the nature and of the residual strain fields and coating morphology had a direct effect on fracture response of the two Al_2O_3 coatings (APS and HVOF) during the indentation process.

- It can be confirmed that AE-monitored indentation experiments may be a feasible addition to classical fractographic analysis to study fracture behavior of thermally sprayed coatings. For materials where cracks are not visible at the fixed resolution chosen, a full measure of crack prevalence would require fractal dimension analysis which is time consuming offering a motivation for AE-based crack monitoring.

References

1. P. Fauchais, M. Fukumoto, A. Vardelle, and M. Vardelle, Knowledge Concerning Splat Formation: An invited Review, *J. Therm. Spray Technol.*, 2004, **13**, p 337-360
2. R. Ahmed, H. Yu, V. Stoica, L. Edwards, and J.R. Santisteban, Neutron Diffraction Residual Strain Measurements in Post-treated Thermal Spray Cermet Coatings, *Mater. Sci. Eng. A*, 2008, **498**, p 191-202
3. R. Ahmed, H. Yu, S. Stewart, L. Edwards, and J.R. Santisteban, Residual Strain Measurements in Thermal Spray Cermet Coatings Via Neutron Diffraction, *ASME J. Tribol.*, 2007, **129**, p 411-418
4. R. Ahmed, N.H. Faisal, S.M. Knupfer, A.M. Paradowska, M.E. Fitzpatrick, K.A. Khor, and J. Cizek, Neutron Diffraction Residual Strain Measurements in Plasma Sprayed Nanostructured Hydroxyapatite Coatings for Orthopaedic Implants, *Mater. Sci. Forum*, 2010, **652**, p 309-314
5. A. Kulkarni, J. Gutleber, S. Sampath, A. Goland, W.B. Lindquist, H. Herman, A.J. Allen, and B. Dowd, Studies of the Microstructure and Properties of Dense Ceramic Coatings Produced by High-Velocity Oxygen-Fuel Combustion Spraying, *Mater. Sci. Eng. A*, 2004, **369**, p 124-137
6. T. Itsukaichi, S. Osawa, and R. Ahmed, *Proc. Int. Therm. Spray Conf. Florida*, C. Moreau and B. Marple, Ed., ASM International, Materials Park, OH, 2003, p 819-824
7. T. Morishita, S. Osawa, and T. Itsukaichi, HVOF Ceramic Coatings, *Proc. Int. Therm. Spray Conf. (Germany), Proc. CD Section: HVOF-Processes and Materials I*, ASM International, Materials Park, OH, 2004, p 1-4
8. D.L. Coats and A.D. Krawitz, Effect of Particle Size on Thermal Residual Stress in WC-Co Composites, *Mater. Sci. Eng. A*, 2003, **359**, p 338-342
9. T.G. Herold, H.J. Prask, and F.S. Biancaniello, *Residual Stresses and Elastic Constants in Thermal Deposits, Recent Advances in Experimental Mechanics*, E.E. Gdoutos, Ed., in Honor of Isaac M. Daniel, Kluwer Academic Publishers, Dordrecht, Netherlands, 2002, p 507-514
10. S. Ahmaniemi, M. Vippola, P. Vuoristo, T. Mäntylä, M. Buchmann, and R. Gadow, Residual Stresses in Aluminium Phosphate Sealed Plasma Sprayed Oxide Coatings and Their Effect on Abrasive Wear, *Wear*, 2002, **252**, p 614-623
11. J. Pina, A. Dias, and J.L. Lebrun, Study by X-ray Diffraction and Mechanical Analysis of the Residual Stress Generation During Thermal Spraying, *Mater. Sci. Eng. A*, 2003, **347**, p 21-31
12. G. Bolelli, L. Lusvarghi, T. Varis, E. Turunen, M. Leoni, P. Scardi, C.L. Cazanza-Ricardo, and M. Barletta, Residual Stresses in HVOF-Sprayed Ceramic Coatings, *Surf. Coat. Technol.*, 2008, **202**, p 4810-4819
13. T. Valente, C. Bartuli, M. Sebastiani, and F. Casadei, Finite Element Analysis of Residual Stress in Plasma-Sprayed Ceramic Coatings, *Proc. Inst. Mech. Eng. L J. Mater. Des. Appl.*, 2004, **218**, p 321-330
14. I. Kraus, N. Ganev, G. Gosmanová, H.D. Tietz, L. Pfeiffer, and S. Böhm, Residual Stress Measurement in Alumina Coatings, *Mater. Sci. Eng. A*, 1995, **199**, p L15-L17
15. O. Kovařík, J. Siegl, N. Nohava, and P. Chraska, Young's Modulus and Fatigue Behavior of Plasma-Sprayed Alumina Coatings, *J. Therm. Spray Technol.*, 2005, **14**, p 231-238
16. O. Kesler, J. Matejicek, S. Sampath, S. Suresh, T. Gnaeupel-Herold, P.C. Brand, and H.J. Prask, Measurement of Residual Stress in Plasma-Sprayed Metallic, Ceramic and Composite Coatings, *Mater. Sci. Eng. A*, 1998, **257**, p 215-224
17. V. Luzin, A. Valarezo, and S. Sampath, Through-Thickness Residual Stress Measurement in Metal and Ceramic Spray Coatings by Neutron Diffraction, *Mater. Sci. Forum*, 2008, **571-572**, p 315-320
18. R. Ahmed, N.H. Faisal, R.L. Reuben, A. Paradowska, M. Fitzpatrick, J. Kitamura, and S. Osawa, Neutron Diffraction Residual Strain Measurements in Alumina Coatings Deposited Via Air Plasma and High Velocity Oxy-Fuel Techniques, *J. Phys: CS*, 2010, **251**, art no. 012051
19. S. Safai, H. Herman, and K. Ono, Acoustic Emission Study of Thermal-Sprayed Oxide Coatings, *Am. Ceram. Soc. Bull.*, 1979, **58**, p 624

Peer Reviewed

20. S.L. Ajit Prasad, M.M. Mayuram, and R. Krishnamurthy, Response of Plasma-Sprayed Alumina-Titania Composites to Static Indentation Process, *Mater. Lett.*, 1999, **41**, p 234-240

21. N.H. Faisal, R.L. Reuben, and R. Ahmed, An Improved Measurement of Vickers Indentation Behaviour Through Enhanced Instrumentation, *Meas. Sci. Technol.*, 2011, **22**, art no. 015703 (18 pp)

22. N.H. Faisal, J.A. Steel, R. Ahmed, and R.L. Reuben, The Use of Acoustic Emission to Characterize Fracture Behavior During Vickers Indentation of HVOF Thermally Sprayed WC-Co Coatings, *J. Therm. Spray Technol.*, 2009, **18**, p 525-535

23. N.H. Faisal, "Acoustic Emission Analysis for Quality Assessment of Thermally Sprayed Coatings," PhD thesis, Heriot-Watt University, 2009

24. N.H. Faisal, R. Ahmed, and R.L. Reuben, Indentation Testing and its Acoustic Emission Response: Applications and Emerging Trends, *Int. Mater. Rev.*, 2011, **56**, p 98-142

25. "Standard Test Method for Vickers Hardness of Metallic Materials," ASTM E 92-82, 1992

26. W.C. Oliver and G.M. Pharr, An Improved Technique for Determining Hardness and Elastic Modulus Using Load and Displacement Sensing Indentation Experiments, *J. Mater. Res.*, 1992, **7**, p 1564-1583

27. M.R. Daymond, M.A.M. Bourke, R.B. Von Dreele, B. Clausen, and T. Lorentzen, Use of Rietveld Refinement for Elastic Macrostrain Determination and for Evaluation of Plastic Strain History From Diffraction Spectra, *J. Appl. Phys.*, 1997, **82**, p 1554-1562

28. L. Edwards, Near-Surface Stress Measurement Using Neutron Diffraction, *Analysis of Residual Stress Using Neutron and Synchrotron Radiation*, M.E. Fitzpatrick and A. Lodini, Ed., Taylor & Francis, London, 2003, p 233

29. P.J. Withers, M.W. Johnson, and J.S. Wright, Neutron Strain Scanning Using a Radially Collimated Diffracted Beam, *Physica B*, 2000, **292**, p 273-285

30. H. Vallen, AE Testing Fundamentals, Equipment, Applications, NDT.net 7, http://www.ndt.net/article/v07n09/05/05.htm, 2002

31. K. Nihara, R. Morena, and D.P. Hasselman, Evaluation of K_{1c} of Brittle Solids by the Indentation Method with Low Crack-to-Indent Ratios, *J. Mater. Sci. Lett.*, 1982, **1**, p 13-16

32. K.M. Liang, G. Orange, and G. Fantozzi, Evaluation by Indentation of Fracture Toughness of Ceramic Materials, *J. Mater. Sci.*, 1990, **25**, p 207-214

33. D.K. Shetty, I.G. Wright, P.N. Mincer, and A.H. Clauer, Indentation Fracture of WC-Co Cermets, *J. Mater. Sci.*, 1985, **20**, p 1873-1882

34. S. Guicciardi, A. Balbo, D. Sciti, C. Melandri, and G. Pezzotti, Nanoindentation Characterization of SiC-Based Ceramics, *J. Eur. Ceram. Soc.*, 2007, **27**, p 1399-1404

35. S. Hao, C.J. Li, and G.J. Yang, Influence of Deposition Temperature on the Microstructures and Properties of Plasma-Sprayed Al_2O_3 Coatings, *J. Therm. Spray Technol.*, 2011, **20**, p 160-169

36. R. Mušálek, O. Kovárík, and J. Matejícek, In Situ Observation of Crack Propagation in Thermally Sprayed Coatings, *Surf. Coat. Technol.*, 2010, **205**, p 1807-1811

37. K.S. Forcey and I. Iordanova, Texture and Residual Stresses in Thermally Sprayed Coatings, *Surf. Coat. Technol.*, 1997, **91**, p 174-182

38. K. Shinoda, M. Demura, H. Murakami, S. Kuroda, and S. Sampath, Characterization of Crystallographic Texture in Plasma-Sprayed Splats by Electron-Backscattered Diffraction, *Surf. Coat. Technol.*, 2010, **204**, p 3614-3618

39. S. Kuroda, Properties and Characterization of Thermal Sprayed Coatings—A Review of Recent Research, *Proc 15th Int. Therm. Spray Conf.* (Nice), 1998, p 539-550

40. T.Y. Tsui, W.C. Oliver, and G.M. Pharr, Influence of Stress on the Measurement of Mechanical Properties Using Nanoindentation: Part I. Experimental Studies in an Aluminum Alloy, *J. Mater. Res.*, 1996, **11**, p 752-759

41. T. Gnaeupel-Herold, H.J. Prask, J. Barker, F.S. Biancaniello, R.D. Jiggetts, and J. Matejicek, Microstructure, Mechanical Properties, and Adhesion in IN625 Air Plasma Sprayed Coatings, *Mater. Sci. Eng. A*, 2006, **421**, p 77-85

42. R. Knight and R.W. Smith, *Thermal Spray Coatings: Research, Design, and Applications*, C.C. Berndt and T.F. Bernecki, Ed., ASM International, Materials Park, OH, 1993, p 607-612

43. T.C. Totemeier and J.K. Wright, Residual Stress Determination in Thermally Sprayed Coatings—A Comparison of Curvature Models and X-ray Techniques, *Surf. Coat. Technol.*, 2006, **200**, p 3955-3962

44. S.C. Gill, "Residual Stress in Plasma Sprayed Deposits," PhD Thesis, Cambridge University, 1993

45. H.M. Soliman and A.F. Waheed, Effect of Differential Thermal Expansion Coefficient on Stresses Generated in Coating, *J. Mater. Sci. Technol.*, 1999, **15**, p 457-462

46. http://www.matweb.com

47. B.R. Lawn and R. Wilshaw, Review, Indentation Fracture: Principles and Applications, *J. Mater. Sci.*, 1975, **10**, p 1049-1081

48. A.A. Griffith, The Phenomena of Rupture and Flow in Solids, *Philos. Trans. R. Soc. Lond. A*, 1920, **221**, p 163-198

49. A.P. Buang, R. Liu, X.J. Wu, and M.X. Yao, Cracking Analysis of HVOF Coatings Under Vickers Indentation, *J. Coat. Technol. Res.*, 2008, **5**, DOI 10.1007/s11998-008-9106-8

50. V. Stoica, R. Ahmed, T. Itsukaichi, and S. Tobe, Sliding Wear Evaluation of Hot Isostatically Pressed (HIPed) Thermal Spray Cermet Coatings, *Wear*, 2004, **257**, p 1103-1124

51. C.B. Ponton and R.D. Rawlings, Vickers Indentation Fracture Toughness Test: Part 1. Review of Literature and Formulation of Standardised Indentation Toughness Equations, *Mater. Sci. Technol.*, 1989, **5**, p 865-872

52. M. Factor and I. Roman, Microhardness as a Simple Means of Estimating Relative Wear Resistance of Carbide Thermal Spray Coatings: Part 1. Wear Resistance of Cemented Carbide Coatings, *J. Therm. Spray Technol.*, 2002, **11**, p 468-481

53. H. Luo, D. Goberman, L. Shaw, and M. Gell, Indentation Fracture Behaviour of Plasma-Sprayed Nanostructured Al_2O_3-13 wt.%TiO_2 Coatings, *Mater. Sci. Eng. A*, 2003, **346**, p 237-245

54. P. Ostojic and R. McPherson, Indentation Toughness Testing of Plasma Sprayed Coatings, *Mater. Forum*, 1987, **10**, p 247-255

55. K. Kapoor, A. Ahmad, A. Laksminarayana, and G.V.S. Hemanth Rao, Fracture Properties of Sintered UO_2 Ceramic Pellets With Duplex Microstructure, *J. Nucl. Mater.*, 2007, **366**, p 87-98

56. J. Akbari, Y. Saito, T. Hanaoka, and S. Enomoto, Acoustic Emission and Deformation Mode in Ceramics During Indentation, *JSME Int. J. Ser. A Mech. Mater. Eng.*, 1994, **37**, p 488-494

57. A.K. Ray, G. Das, N.K. Mukhopadhyay, D.K. Bhattacharya, E.S. Dwarakadasa, and N. Parida, Studies on Indentation Fracture Toughness on Ceramic and Ceramic Composite Using Acoustic Emission Technique, *Bull. Mater. Sci.*, 1999, **22**, p 25-32

58. J.M. Jungk, B.L. Boyce, T.E. Buchheit, T.A. Friedmann, D. Yang, and W.W. Gerberich, Indentation Fracture Toughness and Acoustic Energy Release in Tetrahedral Amorphous Carbon Diamond-Like Thin Films, *Acta Mater.*, 2006, **54**, p 4043-4052

59. X. Chen, J. Yan, and A.M. Karlsson, On the Determination of Residual Stress and Mechanical Properties by Indentation, *Mater. Sci. Eng. A*, 2006, **416**, p 139-149

60. J. Jang, Estimation of Residual Stress by Instrumented Indentation: A Review, *J. Ceram. Process. Res.*, 2009, **10**, p 391-400

61. P.J. Withers and H.K.D.H. Bhadeshia, Residual Stress Part 1—Measurement Techniques, *Mater. Sci. Technol.*, 2001, **17**, p 355-365